



Delft University of Technology

Dayside Upper-Thermospheric Density Fluctuations as Observed by GRACE and GRACE-FO at ~500 km Height

Park, Jaeheung; van den IJssel, Jose; Siemes, Christian

DOI

[10.1029/2022JA030976](https://doi.org/10.1029/2022JA030976)

Publication date

2023

Document Version

Final published version

Published in

Journal of Geophysical Research: Space Physics

Citation (APA)

Park, J., van den IJssel, J., & Siemes, C. (2023). Dayside Upper-Thermospheric Density Fluctuations as Observed by GRACE and GRACE-FO at ~500 km Height. *Journal of Geophysical Research: Space Physics*, 128(1), Article e2022JA030976. <https://doi.org/10.1029/2022JA030976>

Important note

To cite this publication, please use the final published version (if applicable). Please check the document version above.

Copyright

Other than for strictly personal use, it is not permitted to download, forward or distribute the text or part of it, without the consent of the author(s) and/or copyright holder(s), unless the work is under an open content license such as Creative Commons.

Takedown policy

Please contact us and provide details if you believe this document breaches copyrights. We will remove access to the work immediately and investigate your claim.

JGR Space Physics

RESEARCH ARTICLE

10.1029/2022JA030976

Dayside Upper-Thermospheric Density Fluctuations as Observed by GRACE and GRACE-FO at ~500 km Height

Jaehung Park^{1,2} , Jose van den IJssel³ , and Christian Siemes³ 

¹Space Science Division, Korea Astronomy and Space Science Institute, Daejeon, South Korea, ²Department of Astronomy and Space Science, Korea University of Science and Technology, Daejeon, South Korea, ³Faculty of Aerospace Engineering, Delft University of Technology, Delft, The Netherlands

Key Points:

- We investigated dayside upper-thermospheric mass density fluctuations using Gravity Recovery and Climate Experiment (GRACE) and GRACE-FO data at ~500 km height from 2002 to 2022
- Seasonal/longitudinal distributions of the fluctuations bear clear signatures of gravity waves (GWs) originating from the lower atmosphere
- Dayside upper-thermospheric GWs are stronger in the pre-noon hours than in the afternoon

Supporting Information:

Supporting Information may be found in the online version of this article.

Correspondence to:

J. Park,
pj@kasi.re.kr

Citation:

Park, J., van den IJssel, J., & Siemes, C. (2023). Dayside upper-thermospheric density fluctuations as observed by GRACE and GRACE-FO at ~500 km height. *Journal of Geophysical Research: Space Physics*, 128, e2022JA030976. <https://doi.org/10.1029/2022JA030976>

Received 2 SEP 2022

Accepted 6 DEC 2022

Author Contributions:

Conceptualization: Jaeheung Park
Data curation: Jose van den IJssel, Christian Siemes
Funding acquisition: Christian Siemes
Methodology: Jaeheung Park, Jose van den IJssel
Project Administration: Christian Siemes
Resources: Jose van den IJssel
Software: Jaeheung Park
Visualization: Christian Siemes
Writing – original draft: Jaeheung Park

© 2022. The Authors.

This is an open access article under the terms of the [Creative Commons Attribution-NonCommercial-NoDerivs License](https://creativecommons.org/licenses/by/4.0/), which permits use and distribution in any medium, provided the original work is properly cited, the use is non-commercial and no modifications or adaptations are made.

Abstract We statistically investigate fluctuation amplitudes (normalized to the background values) of dayside low-/mid-latitude upper-thermospheric mass density as observed by the Gravity Recovery and Climate Experiment (GRACE) and GRACE-Follow-On (GRACE-FO) spacecraft at ~500 km altitude between 2002 and 2022. There are three new findings in our results. First, the climatology closely replicates previous studies on stratospheric and upper-thermospheric gravity waves (GWs) below the GRACE(-FO) altitudes. For example, in low-latitude regions, the fluctuations are stronger above continents than in the oceanic area. Mid-latitude fluctuations prefer the local winter hemisphere to the summer, and the South American/Atlantic region in June solstice hosts stronger fluctuations than in any other low-/mid-latitude locations or seasons. Fluctuations are more intense under lower solar activity. The above-mentioned consistency of the GRACE(-FO) results with previous lower-altitude GW studies confirms that GWs can penetrate up to 500 km. Second, the anti-correlation of upper-thermospheric GW with solar activity, which has been earlier reported for multi-year time scales, can also be identified on the scale of the solar rotation period (~27 days). Third, we demonstrate asymmetry between pre-noon and post-noon GWs. The former exhibits stronger GW activity, which may result from the colder thermosphere being more favorable for intense mass density fluctuations via secondary/tertiary GW generation.

1. Introduction

1.1. Backgrounds

Gravity waves (GWs) represent traveling atmospheric oscillations generated by initial perturbation in the presence of restoring force by the Earth's gravity. The GWs are driven by various mechanisms, such as tropospheric convection (e.g., Ern et al., 2011), orography (e.g., Hoffmann et al., 2013), frontal systems (e.g., Moffat-Griffin et al., 2020, and references therein), and jet streams (e.g., Song et al., 2021). In the stratosphere, the GW climatology generally exhibits the following features. Near the equator (especially in the summer hemisphere), GWs are stronger in the continental regions than above the oceans, which is usually attributed to strong tropospheric convection in the former area (e.g., Geller et al., 2015, Figures 1 and 2; Hocke et al., 2016, Figure 6). At mid-latitudes, GW intensity is higher in the winter hemisphere than in the summer, for which stratospheric jets blocked by high mountains (e.g., the Andes) play an important role (e.g., Hoffmann et al., 2013, Figures 6 and 7; Hocke et al., 2016, Figure 6). The stratospheric GW activity exhibits anti-correlation with solar activity proxies, such as the $F_{10.7}$ index (e.g., Ern et al., 2011; X. Liu, Yue, et al., 2017) although quantitative difference among different studies may exist due to the limitation of each data set (e.g., covering less than or only slightly more than one solar cycle), the presence of other long-term oscillations in the Earth system, or the different instruments and methods used.

In the last decades, the GW signatures were reported also in the upper-thermosphere (above 150 km altitudes; see Qian et al., 2018) in quiet-time low-/mid-latitude regions. Using the Gravity field and steady-state Ocean Circulation Explorer (GOCE) data, Forbes et al. (2016), Garcia et al. (2016), H. Liu, Pedatella, and Hocke (2017), and Xu et al. (2021) reported GW signatures at ~250 km altitudes. With the Challenging Minisatellite Payload (CHAMP) observations at ~400 km between 2001 and 2010, Park et al. (2014) demonstrated that the climatology of upper-thermospheric density fluctuations closely follows that of stratospheric GWs. Until now, the highest altitude for which thermospheric GW climatology was investigated was the CHAMP height (mainly <450 km); for example, Trinh et al. (2018) and Xu et al. (2021).

Writing – review & editing: Jose van den IJssel, Christian Siemes

1.2. Room for Further Improvements Over Previous Studies on Upper-Thermospheric Gravity Waves

Though GWs in the upper thermosphere (>150 km) have been investigated during the last 10 years, there is still room for improving our knowledge about the phenomena. The highest altitude for which thermospheric GW statistics were constructed was that of CHAMP (below ~450 km). There are not yet reports in literature which demonstrate that GW signatures are identifiable at higher altitudes, such as at ~500 km. CHAMP was ~50 km below the above-mentioned 500 km at the beginning of the mission (during the solar maximum years around 2002) and more than 100 km below in the second half of the mission (near the solar minimum in 2009): GW activity was stronger for the latter than for the former (e.g., Park et al., 2014). The altitude difference between the 500 km and that of CHAMP (i.e., an approximate difference of 50~150 km) is not negligibly small. Upper-thermospheric GWs can lose half of their momentum flux when they propagate upward by several tens of kilometers (\approx atmospheric scale height): for example, by 30 km under low solar activity (Vadas, 2007, Section 4). The CHAMP altitude under low solar activity (2006–2010) was ~350 km (Xu et al., 2021, Figure 1b; Stolle, Olsen, et al., 2021; Stolle, Michaelis, et al., 2021, Figure 1), which is roughly 5 scale heights below 500 km ($500 - 350 \text{ km} = 150 \text{ km} = 5 \times 30 \text{ km}$). Then, the momentum flux of GWs at 500 km would be only $2^{-5} \approx 1/32 \approx 3\%$ of that at CHAMP heights (i.e., attenuation by ~97%) under low solar activity. Hence, the observability of GWs at 500 km, especially under low solar activity, cannot be trivially deduced from CHAMP measurements, but should be verified with an independent data set.

Second, while the anti-correlation of upper-thermospheric GWs with solar activity has been reported in the past, existing studies generally tackled the topic by classifying multi-year observation data into 2 ~ 3 coarsely gridded solar activity bins (e.g., Garcia et al., 2016; Park et al., 2014). To the best of the authors' knowledge, it is yet to be answered whether the anti-correlation reported earlier remains valid even on the time scale of the ~27-day solar rotations: that is, whether the response of upper-thermospheric GWs to solar activity is agile enough to track the ~27-day periodicity.

Third, the local time dependence of upper-thermospheric GWs needs to be studied because this topic was not thoroughly investigated before. For example, GOCE was fixed to the dawn-dusk meridian due to its Sun-synchronous orbit. Illés-Almár et al. (2001, Figure 2) showed local time dependence of thermospheric wave-like structures. However, except that the nighttime fluctuations are stronger than dayside ones, no detailed discussion was given. The latitudinal coverage of their data set was also limited to the near-equatorial regions (at most 5° in geographic latitudes). Though CHAMP could cover a wide latitude range and all the local time sectors during its orbit precession, detailed dependence of upper-thermospheric GWs on local time was not reported in previous papers.

In addition, the longest data set used in existing studies of upper-thermospheric GWs was that of CHAMP (spanning slightly less than one decade; 2001–2010). Extending the data set to a longer period, for example, 2 decades, will allow us to exhaustively validate the current knowledge on upper-thermospheric GWs.

In the following sections, we will address the above-mentioned missing pieces of the puzzle about the upper-thermospheric GWs: (a) their climatology near 500 km, (b) the solar activity dependence of GWs on ~27-day time scales, and (c) the GW activity changes with local time. Section 2 describes the spacecraft and instruments that will be used, as well as strategies for data processing. Statistical results of upper-thermospheric GWs are given in Section 3, which will be discussed in the context of previous papers in Section 4. Finally, Section 5 briefly recapitulates the main findings and draws conclusions.

2. Spacecraft, Instruments, and Data Processing

2.1. Spacecraft and Instruments: GRACE and GRACE-FO

The Gravity Recovery and Climate Experiment (GRACE) mission is composed of twin spacecraft (GRACE-A and GRACE-B) that were launched on 17 March 2002 into a polar (inclination angle ~89°) circular (initial altitude ~500 km) orbit. As mentioned before, the observation altitude is higher than previously explored altitude ranges for GW climatology. Besides, due to the higher initial altitude, the descent due to atmospheric drag is slower for the GRACE mission than for lower-altitude spacecraft, such as CHAMP. These features are concisely summarized in Figure 1, where altitude evolutions of GRACE and other missions are given with different colors (Figure 1a) as well as $F_{10.7}$ index during the period of interest (Figure 1b). Each of the GRACE satellites carried a three-axis accelerometer that can precisely measure the spacecraft's acceleration. From the non-gravitational

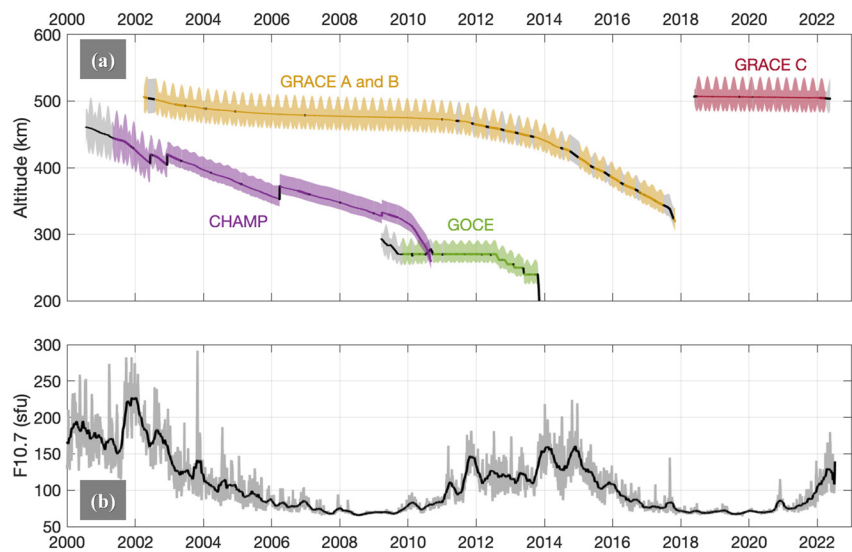


Figure 1. (a) Altitude evolution of Gravity Recovery and Climate Experiment (GRACE-A and GRACE-B; orange) and GRACE-FO (GRACE-C; red) in the context of other missions that were used in previous studies of upper-thermospheric gravity waves, such as Challenging Minisatellite Payload (purple) and GOCE (green). The colored shades represent the actual altitudes reflecting the apogees and perigees while the colored solid curves correspond to the representative altitudes. The gray parts of the altitude evolution indicate periods where no data of upper-thermospheric mass density exist at the Delft University of Technology's thermosphere database (<http://thermosphere.tudelft.nl>). (b) Evolution of solar activity ($F_{10.7}$ index). The gray lines are actual daily indices while the 81-day moving averages are shown with the black curve.

component of the acceleration, in combination with precise orbit information based on the Global Navigation Satellite System, one can estimate thermospheric mass density and cross-track wind in situ (e.g., Doornbos, 2012; Doornbos et al., 2010; Van den IJssel, 2014). The GRACE mission came to a successful end in March 2018. Almost immediately afterward, in May 2018, another pair of spacecraft named the GRACE Follow-On (GRACE-FO; GRACE-C and GRACE-D) was launched to inherit the duty of GRACE. The GRACE-FO altitudes are similar to those of GRACE (~500 km) at the launch as shown in Figure 1a: see also Landerer et al. (2020), Stolle, Olsen, et al. (2021), and Stolle, Michaelis, et al. (2021). GRACE and GRACE-FO spacecraft carry similar accelerometers manufactured by the same institute (Christophe et al., 2015).

Recently, the Thermosphere Observations from Low-Earth Orbiting Satellites (TOLEOS) project sponsored by the Swarm Data, Innovation, and Science Cluster (DISC) via the European Space Agency (ESA) has retrieved the density and wind data from both GRACE and GRACE-FO measurements, which are open to the public at the ESA's Swarm repository (<https://swarm-diss.eo.esa.int/#swarm%2FMultimission>) and the Delft University of Technology's thermosphere database (<http://thermosphere.tudelft.nl>). The data rate is 0.1 Hz, that is, with one data point every 10 s. Detailed descriptions of the product are available in Siemes and the TOLEOS team (2022). In the current study, we focus on the thermospheric mass density data of the GRACE-A and GRACE-C spacecraft. Together, the GRACE-A and GRACE-C measurements cover the period between April 2002 and April 2022 (as of August 2022) nearly seamlessly, as shown in Figure 1a.

We note that GRACE-B was nearly co-located with GRACE-A with the inter-satellite horizontal distance of only about 220 km (i.e., the two data sets are largely redundant for the purpose of thermosphere density monitoring) and ended earlier than GRACE-A. GRACE-D density data are unavailable due to accelerometer issues (e.g., Behzadpour et al., 2021; Landerer et al., 2020), which make the use of these data unsuitable for gravity field recovery, as well as for density retrieval. These are the rationale for using only GRACE-A and GRACE-C observations in this study. As for cross-track wind measurements, just a limited amount of thermospheric wind data are currently available at the TOLEOS project repository: data in 2011–2017 for GRACE and no data at all for GRACE-FO. It is because meaningful wind data can be obtained only when aerodynamic acceleration is strong enough (see also Section 4.2.4 in Doornbos, 2012). For GRACE, this is the case only for the second half of the mission (around 2011–2017), when the spacecraft was at low altitudes under high solar activity. For GRACE-FO, the current observations are not suited for wind retrieval. It is expected that in the near future the GRACE-FO will

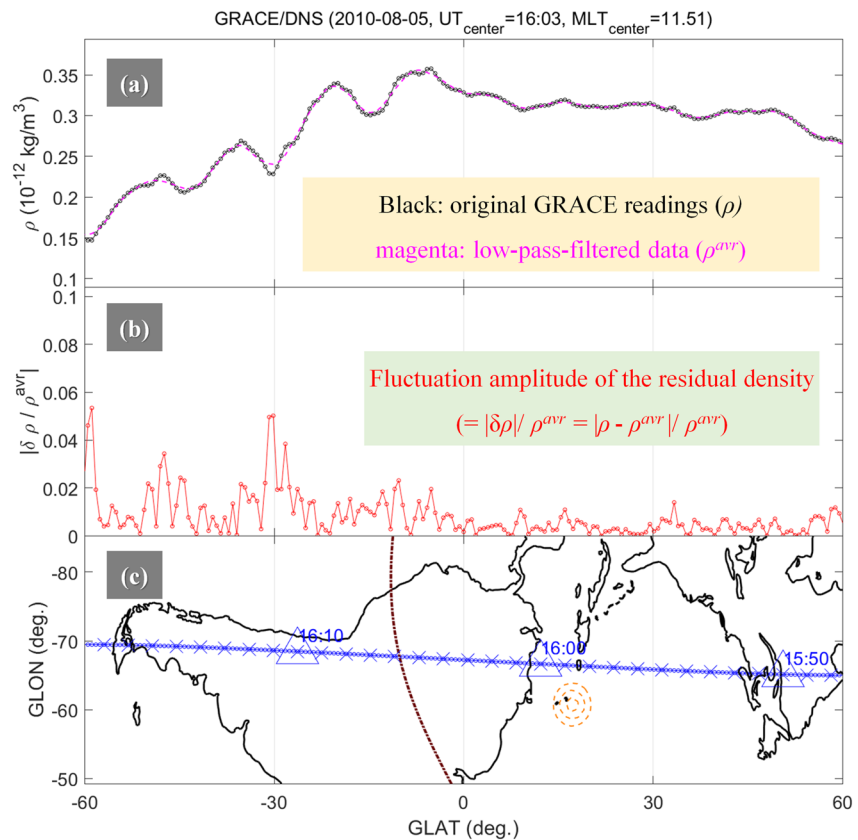


Figure 2. An example demonstrating how to extract fluctuating components from the thermospheric mass density observed by Gravity Recovery and Climate Experiment (GRACE). In panel a, the black curve with symbols is the original reading from GRACE data files while the magenta dashed line is the ambient density extracted by applying a Savitzky-Golay smoothing filter. Panel b presents the amplitude of the density residual between the two curves in panel a, which is normalized by the ambient density: that is, the residual amplitude is represented as a fraction of the ambient value. Panel c is a world map rotated clockwise by 90°, with the GRACE trajectory shown in blue. The crosses on the orbit are given every minute while the triangles are every 10 min. For context, the dip equator is marked with the thick dot-dashed line, and the dashed orange ovals denote the sub-solar point (solar zenith angle = 0°).

experience larger aerodynamic signals due to the decreasing altitude and the increasing solar activity, which will allow the retrieval of wind data from the accelerometer observations.

2.2. Data Processing Strategies

To extract *background* thermospheric density (ρ_{avr}), we apply a Savitzky-Golay filter (order = 3, window size = 17 data points = 170 s ~1,275 km) to the GRACE(-FO) readings. This value was chosen as a trade-off between minimizing spectral loss of low-frequency components and avoiding possible contamination from terminator waves (wavelength ~3,000 km; Forbes et al., 2008). In Figure 2a, the black curve with symbols represents the original readings (ρ) from GRACE data files, while the magenta dashed one corresponds to the filtered data (ρ_{avr}). Then, the absolute values of the residual between the original and filtered data ($=|\delta\rho| = |\rho - \rho_{avr}|$; hereafter, “*absolute fluctuation amplitude*”) are calculated and normalized by the ambient density (ρ_{avr}): the result ($|\delta\rho/\rho_{avr}|$) is shown in Figure 2b. We deem the $|\delta\rho/\rho_{avr}|$ (hereafter, “*relative fluctuation amplitude*”) as representing undulation levels of upper-thermospheric mass density. Locations of the GRACE observations are shown in Figure 2c in blue color: crosses are shown every minute, and triangles are every 10 min. The background of Figure 2c is the world map rotated clockwise by 90°, as well as the dip equator (dot-dashed line) and subsolar point (dashed orange ovals). In the statistics that will be presented in the following sections, we show bin averages of the *relative fluctuation amplitude* at different locations and under different geophysical conditions (e.g., different local times, seasons, and solar activities).

Throughout this paper, we use three Lloyd seasons (e.g., Matzka et al., 2021) that are defined as follows. The June solstice consists of the month from May to August. Periods from November to February next year constitute the December solstice. The remaining months belong to the combined equinoxes. As for local time, we use magnetic local time (MLT) following Liu et al. (2005) and calculate it in the quasi-dipole coordinate system (Laundal & Richmond, 2017). In this paper, we define that high and low solar activity periods have $F_{10.7}$ indices above and below 90, respectively. To focus on the quiet-time climatology of GWs, we neglect daily GRACE(-FO) data files whenever the maximum Kp index on that day is larger than 4.0. However, the high- Kp data are used for the daily average plots of Figures 5 and 6 (otherwise, unwanted data gaps appear), which will be presented later in this paper. Also, daily files containing no more data points than the Savitzky-Golay filter size (17 data points) are omitted from the statistics. For data quality control, non-positive mass density or values at and above 10^{-10} kg/m³ are considered unreasonable and, therefore, are neglected before we apply the filter. To avoid possible contamination by data jumps or time gaps, we first group neighboring data points of high fluctuations ($|\delta\rho/\rho_{\text{avr}}| > 2\%$) unless they are separated by >10 data points of low fluctuations ($|\delta\rho/\rho_{\text{avr}}| \leq 2\%$). If a high-fluctuation group contains either a time gap or suspicious data points whose *relative* fluctuation amplitudes are $>100\%$, the whole group is deemed contaminated and put aside from the statistics. A group is also neglected if it is too short (<10 data points): those groups may have been affected by a few outliers. Through the procedure of data length and quality control, about 3.3% (~ 2 million) of the data points (~ 56 million in total) are discarded. The discarded data points are categorized as follows: (a) 0.88% of the 56 million is unreasonably high raw data (larger than 10^{-10} kg/m³), (b) 0.05% is non-positive (zero or negative), (c) 0.56% is high-fluctuation groups containing data gaps, (d) 1.8% is high-fluctuation groups that are too short (<10 data points), and (e) 0.03% is high-fluctuation groups including unreasonable amplitude ($>100\%$ of ρ_{avr}).

There are two points worth noting before getting into the statistical results. First, only *daytime* (i.e., mainly 07–17 MLT) GRACE(-FO) measurements are used in this study. We want to focus on GWs coming from the lower atmosphere while *nighttime* thermospheric density can be disturbed by ionospheric irregularities generated in the F-region (e.g., Illés-Almár et al., 1998; Park et al., 2010) or very strong terminator waves (e.g., Forbes et al., 2008, Figure 2). Second, we concentrate on low-/mid-latitude data (generally equatorward of $\pm 60^\circ$ in geographic latitudes). The high-latitude thermosphere may be affected not only by GWs coming from below, but also by energy deposition from outer space (e.g., Bruinsma & Forbes, 2008; Lühr et al., 2004). In summary, the statistics in the following Sections are relevant to the dayside low-/mid-latitude thermosphere around 500 km height.

3. Results

3.1. Seasonal/Longitudinal Variation of GWs

Figure 3 presents the *relative* fluctuation amplitude of thermospheric mass density as observed by GRACE and GRACE-FO during 2002–2022. The thick white line represents the dip equator. Each pixel spans 2° in geographic latitude (GLAT) and 2° in geographic longitude (GLON). Figure 3 is obtained by applying a 5-by-5 median filter to the raw pixel maps of the *relative* fluctuation amplitude, for the sake of visual clarity. As can be seen in the color bar on the right-hand side, the amplitudes are given in a logarithmic scale to facilitate display of a wide dynamic range. The lowest (dark blue) and highest (dark red) color levels span a range slightly wider than one order of magnitude, that is, the difference between the two extreme colors is a little larger than “+1” in the base-10 logarithm. Each panel in Figure 3 corresponds to one season: (a) combined equinoxes, (b) June solstice, and (c) December solstice. As mentioned in the previous section, only daytime data between 07 and 17 MLT are used, as annotated inside each panel.

Figure 3, which is relevant to the altitude of ~ 500 km, replicates well the upper-thermospheric GW climatology as reported in previous studies based on CHAMP (~ 400 km altitude) and GOCE (~ 250 km altitude) data, while quantitative differences may exist due to different data processing methods (e.g., filter sizes) and/or instrument calibration (e.g., gas-surface interaction models), as we will discuss later in Section 4. First, we observe that low-latitude (e.g., $|\text{GLAT}| < 10^\circ$) GWs are stronger above the continents than above the oceans. The continent/ocean asymmetry is conspicuous in Figure 3a (combined equinoxes) and 3c (December solstice) while that in Figure 3b (June solstice) is slightly blurred, with a global enhancement of fluctuations during that season. Still, a noticeable local minimum of fluctuations is seen above the Eastern Pacific region (i.e., to the west of America) for all three seasons. Second, mid-latitude (e.g., $|\text{GLAT}| > 20^\circ$) GWs are stronger in the local winter hemisphere, that is, in the Northern Hemisphere (NH) during December solstice (Figure 3c) and in the Southern

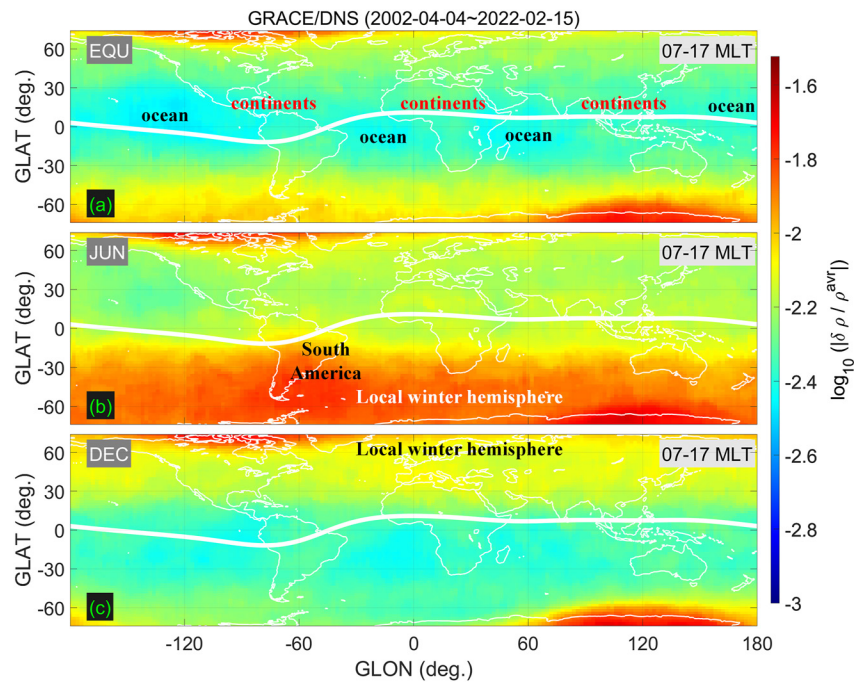


Figure 3. Statistical maps of the *relative* fluctuation amplitude of thermospheric mass density measured by GRACE(-FO): (a) combined equinoxes, (b) June solstice, and (c) December solstice. The thick white curve represents the dip equator.

Hemisphere (SH) during June solstice (Figure 3b). Especially, the South American/Atlantic area during June solstice (Figure 3b) hosts stronger GWs than in any other low-/mid-latitude locations or seasons. Considering the consistency between Figure 3 and previous GW studies, hereafter we deem the *relative* fluctuation amplitude of GRACE(-FO) thermospheric mass density as GW activity or GW intensity. While the Canadian Arctic and Australian Antarctic regions at high latitudes exhibit strong fluctuations (dark red color), they cannot be solely attributed to GWs originating from below the thermosphere. As mentioned in Section 2, strong in situ drivers of thermospheric perturbation are known to reside at high latitudes (e.g., Lühr et al., 2004), which are different from the main topic of this study.

3.2. Solar Activity Dependence of GWs

Figure 4 is similar to Figure 3, but with each column corresponding to a different level of solar activity ($F_{10.7}$ index). The left column represents high solar activity ($F_{10.7} \geq 90$) while the right one belongs to low solar activity ($F_{10.7} < 90$). The respective columns generally replicate the three main features of GW climatology that were already shown in Figure 3. Despite the qualitative resemblance, the GW activity is much stronger in the low solar activity (right column) than during the high solar activity (left column). Visual inspection indicates that the difference between the two columns is less than one order of magnitude (i.e., less than the span of the whole color bar). In other words, GW activity under low solar activity conditions is several times stronger than under high solar activity.

Figure 5 presents the solar cycle dependence of the GWs more quantitatively. In Figure 5a, each small dot corresponds to a daily average of low-latitude ($|\text{GLAT}| < 10^\circ$) GW activity between 07 and 17 MLT. The thick curve is the moving median of the dots: the window size is 160 days, which is the approximate time needed for GRACE(-FO) to cover all MLT sectors (e.g., Lühr & Xiong, 2010). We take the moving median to damp down MLT-dependent (or precession-induced) apparent variations of GW intensity (i.e., the 160-day oscillations of the small dots) to focus on the true solar cycle dependence of GWs. Figure 5b is similar to Figure 5a, but for mid-latitude ($|\text{GLAT}| = 20^\circ \sim 45^\circ$) regions. We have chosen the lower boundary of the mid-latitude range (i.e., $|\text{GLAT}| = 20^\circ$) to conservatively avoid overlap between the low- (Figure 5a) and mid-latitude (Figure 5b) regions. Figures 5c and 5d are similar to Figures 5a and 5b, but with daily averaged ρ instead of $|\delta\rho/\rho_{\text{avr}}|$. The apparent discontinuity in Figures 5c and 5d in 2018 is due to the gap between the GRACE end of science operations in

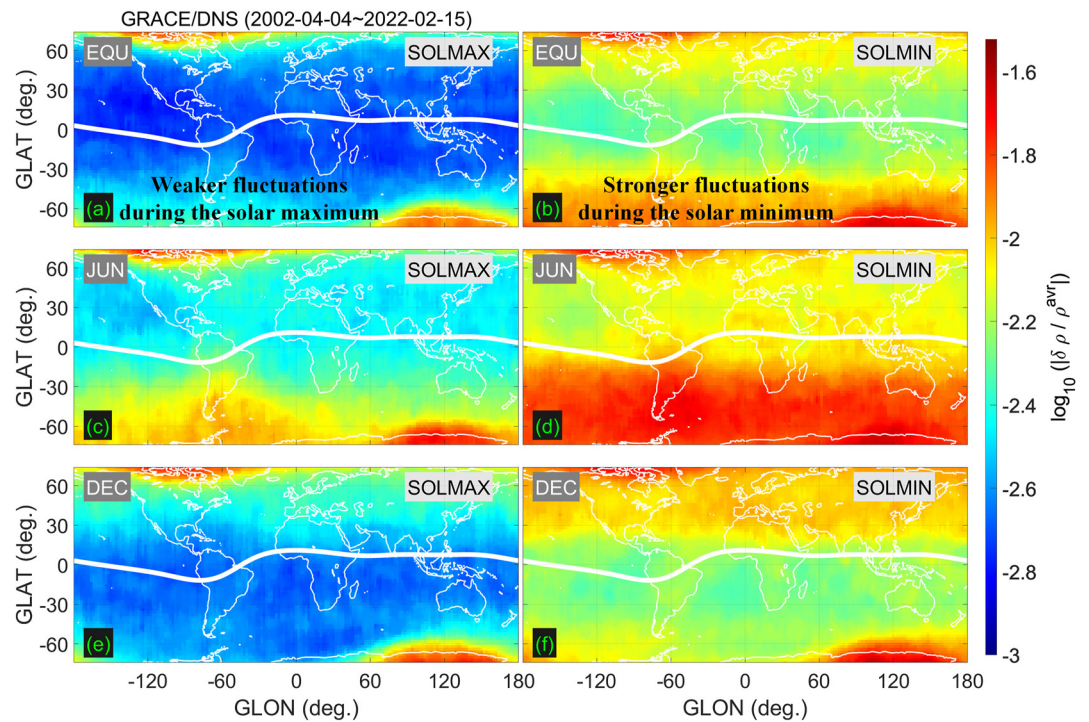


Figure 4. Similar to Figure 3, but for different solar activities on different columns. The left and right columns represent the high and low solar activity that correspond to $F_{10.7}$ indices above and below 90, respectively.

October 2017 and the GRACE-FO launch in May 2018, which were at different altitudes from each other at that time (see Figure 1). Dots in Figure 5e present daily $F_{10.7}$ indices, while the thick curve is obtained with the same moving-average filter as was applied to the other panels. For both low- and mid-latitude regions (Figures 5a and 5b), we can see that GW activities are strongly anti-correlated with $F_{10.7}$. The correlation coefficient (R) between the thick curves between Figure 5a (low-latitude GW) and 5e ($F_{10.7}$) is -0.74 , as is annotated inside Figure 5a. Similarly high anti-correlation is found for Figure 5b (mid-latitude GW; $R = -0.71$). On the contrary, the ρ climatology in Figures 5c and 5d does not exhibit as good correlation with $F_{10.7}$. The IRI is below 0.4, which is largely attributable to the strong altitude decay of GRACE after 2012 and the change between GRACE and GRACE-FO (at different altitudes) in 2018. In Figures 5a and 5b, average GW activity during solar maxima generally stays at a level of ~ 0.002 , while that of solar minima approximately varies between 0.007 and 0.01, depending on GLAT ranges (low- or mid-latitudes) and solar cycles (i.e., 2008–2009 or 2019–2020). Therefore, GW activity during solar minima is roughly 3–5 times stronger than during solar maxima.

The $F_{10.7}$ dependence of GW activity can also be seen on the ~ 27 -day time scale of solar rotation. Note that the ~ 27 -day scale is much shorter than the 160 days needed for GRACE to cover all the MLT sectors as mentioned above: the two signals can be disentangled by visual inspection. The left and right columns of Figure 6 present GRACE data during two different periods: (left) 2002–2003 and (right) 2005. The top four panels present (a and b) the representative MLT of the GRACE data used, (c and d) Kp , (e and f) Dst, and (g and h) $F_{10.7}$ indices, respectively. In Figures 6g and 6h, the oscillating $F_{10.7}$ index represents solar rotation with a period of ~ 27 days. As can be seen in the MLT coverage in the top row, each column in Figure 6 only spans a limited time (~ 140 days), which is shorter than the 160 days needed for GRACE half-precession. The fifth and seventh rows show upper-thermospheric mass density measured by GRACE (ρ) and the relative fluctuation amplitude ($\delta\rho/\rho_{avr}$), respectively, as a function of GLAT (vertical axis) and date (horizontal axis). The sixth and eighth rows correspond to the latitudinal average of the fifth and seventh rows, respectively. Annotating rectangles are added to guide the readers' eyes. In the bottom two rows (Figures 6m–6p) we can see that the GW activity exhibits anti-phase variations with $F_{10.7}$ (Figures 6g and 6h) on the time scale of ~ 27 days. The GW intensity decreases (i.e., becoming deeper blue in Figures 6m and 6n) whenever the $F_{10.7}$ index peaks. This is the first time that the relationship between upper-thermospheric GW activity and $F_{10.7}$ has been reported on such a short time scale.

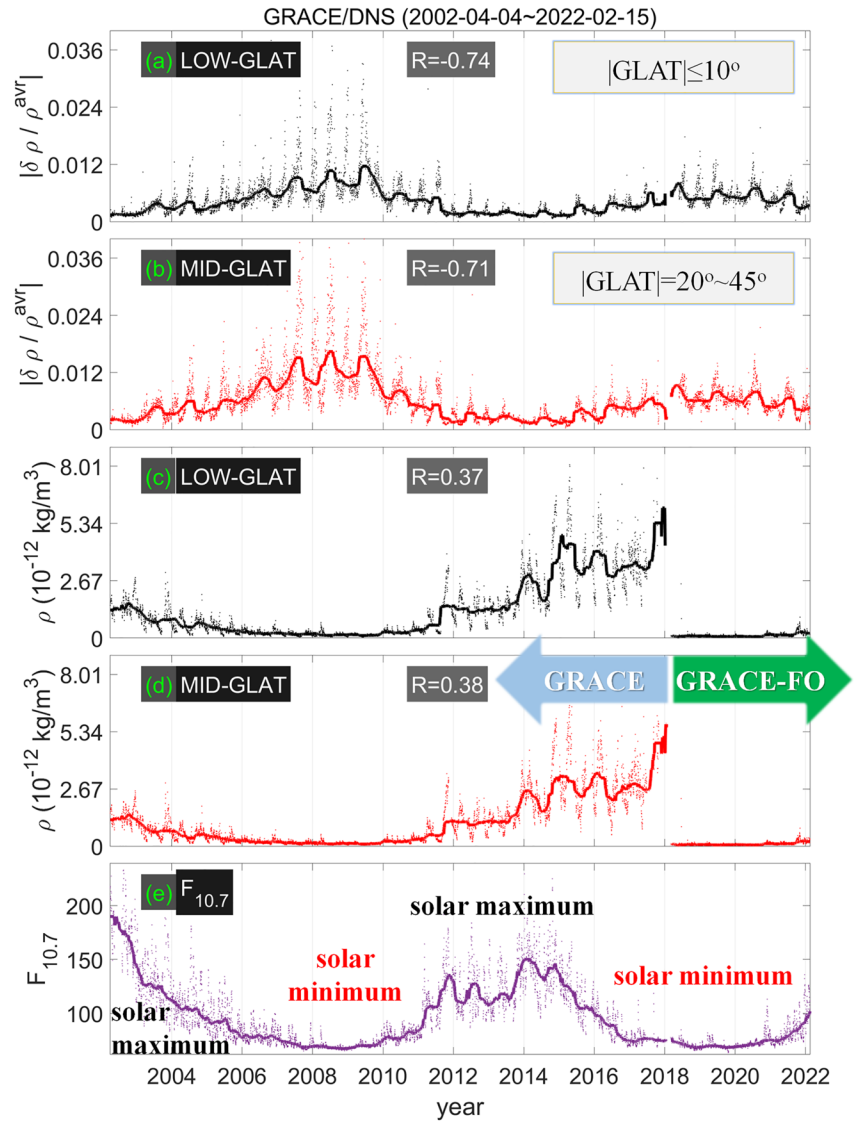


Figure 5. In panels a and b, the small dots represent daily-averaged *relative* fluctuation amplitude of dayside (07–17 Magnetic Local Time) thermospheric density: (a) low-latitude region ($|GLAT| < 10^\circ$), and (b) mid-latitude region ($|GLAT| = 20^\circ \sim 45^\circ$). Panels c and d are similar to panels a and b, but with the *relative* fluctuation amplitude replaced by daily averaged ρ . Dots in panel e correspond to the daily $F_{10.7}$ index. The thick curve in each panel is the 160-day (i.e., the time needed for Gravity Recovery and Climate Experiment and GRACE-FO to cover all the local times) moving median of the dots.

3.3. Local Time Dependence of GWs

In this subsection, we investigate the dependence of GW activity on MLT. Figure 7 is similar to Figure 4, but with each column corresponding to an MLT sector. The left column is for pre-noon hours (07–12 MLT) while the right one is for post-noon (12–17 MLT). Each of the two columns agrees well with the full GW climatology that was shown in Figure 3: for example, low-latitude GWs staying largely above the continents, mid-latitude GWs preferring the winter hemisphere, and the conspicuous hotspot in the South American/Atlantic region during June solstice. Besides the morphological similarity, we can see that the GW activity is much stronger before noon (left column) than afterward (right column).

Figure 8 gives a slightly different perspective on the MLT dependence of GW activity. It is similar to Figure 4 (i.e., with the left and right columns corresponding to different solar activity), but the horizontal axis is now changed from GLON (Figure 4) to MLT (Figure 8). Within each panel, the left and right halves correspond to the

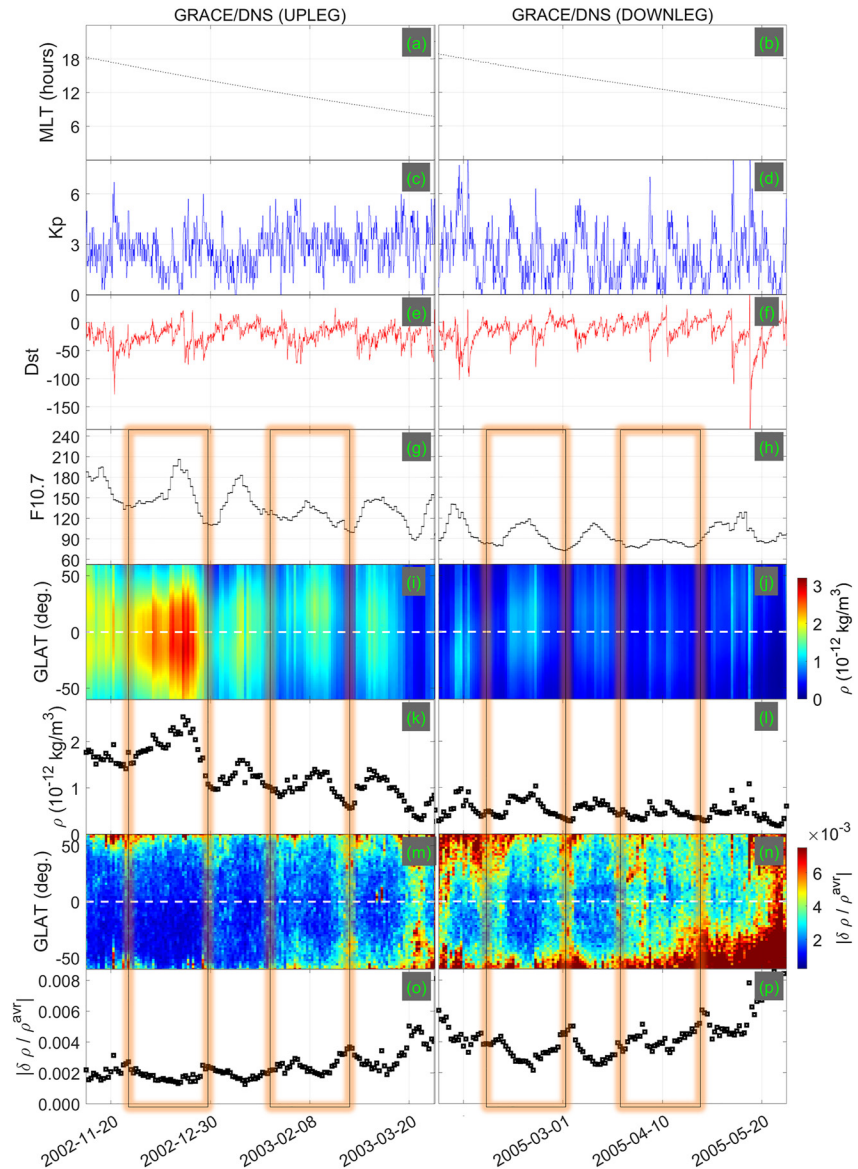


Figure 6. Examples of 27-day variations of upper-thermospheric gravity wave activity. The left and right columns correspond to different periods of observations: (left) 2002–2003 and (right) 2005. The top four rows respectively show the representative Magnetic Local Time of the used Gravity Recovery and Climate Experiment data, K_p , Dst , and $F_{10.7}$ indices. The fifth row presents upper-thermospheric mass density as a function of geographic latitude (vertical axis) and date (horizontal axis). The sixth row shows the latitudinal average of the fifth row. The seventh and eighth rows are similar to the fifth and sixth, but with *relative* fluctuation amplitude instead of the mass density. Rectangles are placed to guide readers' eyes.

pre-noon and post-noon hours, respectively: see the arrowed annotations on the top right of Figure 8. The vertical dotted white lines represent 07, 12, and 17 MLT, which respectively correspond to the nominal start, center, and end of the dayside local time range that was used for Figures 3, 4, and 7. The horizontal dashed white line marks the geographic equator. Figure 8 is fully consistent with previous figures. Mid-latitude GW activity is stronger in the local winter hemisphere (Figures 8c–8f). The years with low solar activity (right column) accommodate more intense GWs than the years with high solar activity (left column). Furthermore, within each panel GWs are generally stronger before noon than afterward, which agrees with Figure 7. To the best of the authors' knowledge, such pre-noon/post-noon asymmetry of upper-thermospheric GWs was not yet reported in previous papers: it is a new finding of this study. In Figure 8, daytime minima of GW activity (bluish colors) are roughly located near 15 MLT and biased toward the local summer hemisphere (e.g., Figures 8d and 8f).

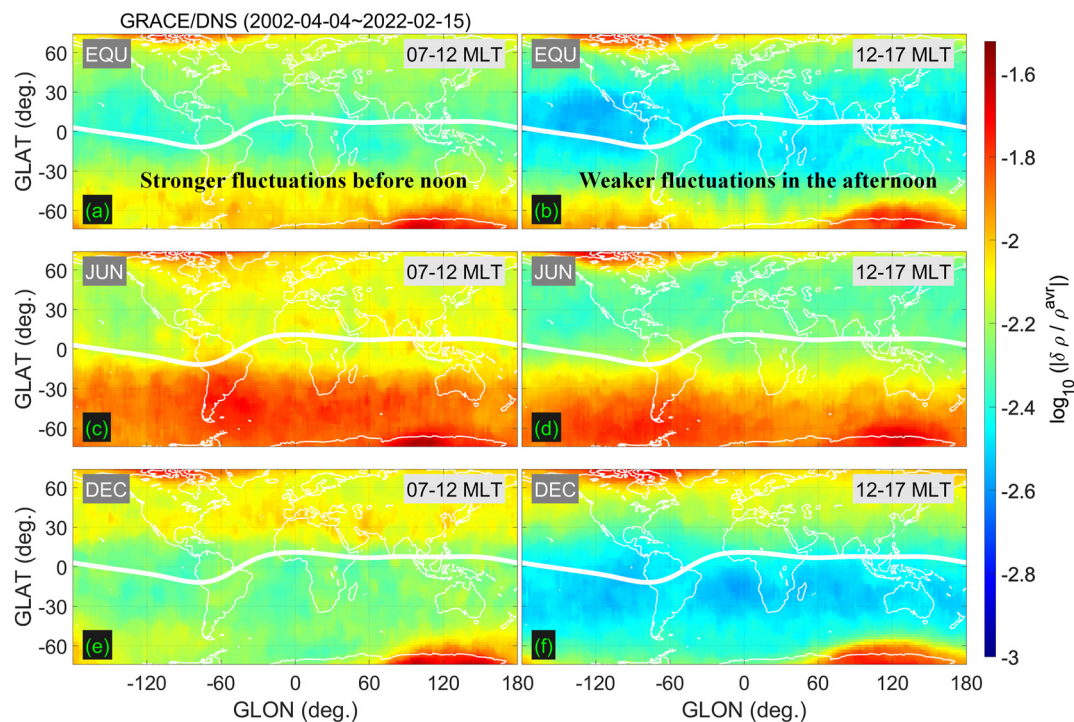


Figure 7. Similar to Figure 3, but for different MLTs on different columns. The left column represents pre-noon hours (07–12 magnetic local time (MLT)), and the right column denotes the post-noon period (12–17 MLT).

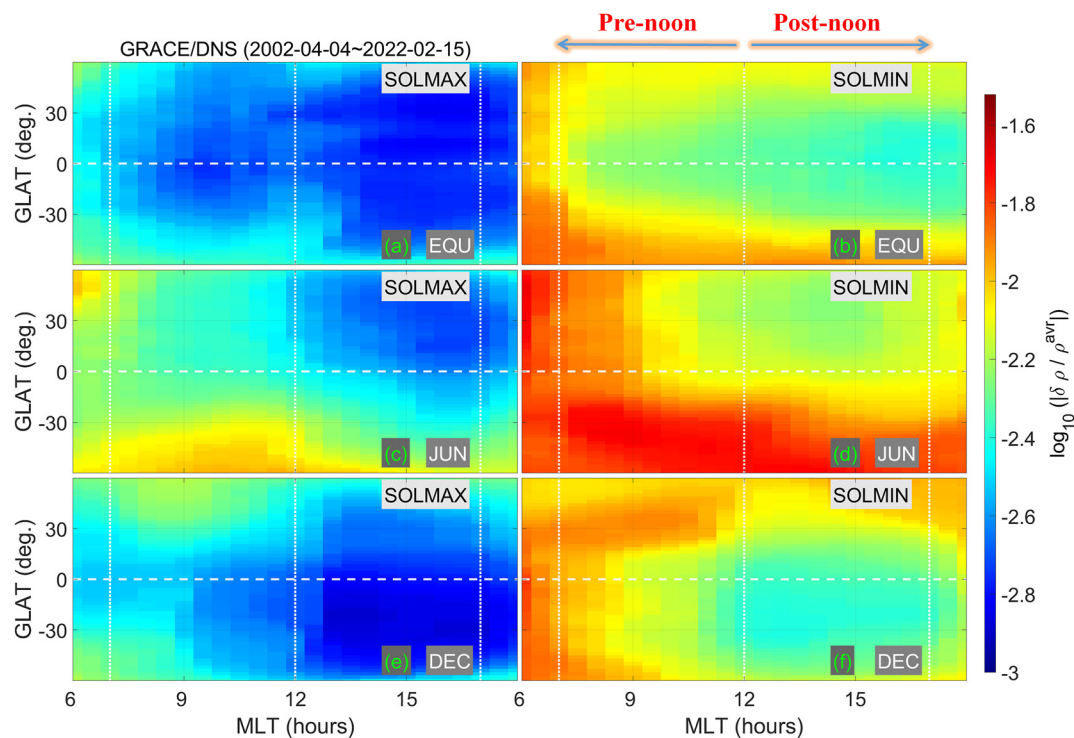


Figure 8. Similar to Figure 4, but with the horizontal axis being magnetic local time (MLT) instead of geographic longitude. The horizontal white dashed line points to the geographic equator, and the vertical dotted lines mark 07 MLT (the earliest MLT used for our dayside statistics shown in Figures 3, 4, and 7), local noon, and 17 MLT (the last MLT used for Figures 3, 4, and 7).

4. Discussion

4.1. Comparison With Previous Studies

In this section, we discuss the GRACE(-FO) observation results in Section 3 in the context of previous studies on upper-thermospheric GWs. First of all, the anti-correlation between upper-thermospheric GW and $F_{10.7}$ (Figures 4 and 5) agrees with previous studies, such as Garcia et al. (2016, Figure 11) and Park et al. (2014). While the two papers coarsely sub-categorize their data into 2–3 solar activity levels, our Figure 5 more quantitatively shows the tight correlation between solar activity and upper-thermospheric GW activity. The correlation coefficients of $F_{10.7}$ with both low- and mid-latitude GWs are stronger (i.e., more negative) than -0.7 .

As mentioned previously in Section 3, the GW activity during solar-minimum years (e.g., 2008 and 2019) is approximately 3–5 times stronger than during solar-maximum years (e.g., 2002 and 2014). This range (a factor of 3–5) is largely consistent with the “factor of two” changes reported by Park et al. (2014). Note that the result of Park et al. (2014) was obtained from the ratio between multi-year averages (i.e., 2001–2005 vs. 2006–2010). On the contrary, the factor of 3–5 in our Figure 5 was estimated from single years near the solar maxima and minima.

Now we discuss the origin of the solar activity dependence of upper-thermospheric GWs. As for stratospheric GWs, Ern et al. (2011) reported an increase in GW activity of less than 20% from a solar maximum to a minimum. Therefore, the large changes of upper-thermospheric GWs in Figure 5 (i.e., a factor of 3–5) point to $F_{10.7}$ -dependent *propagation* efficiency of GWs to the upper thermosphere (other than the $F_{10.7}$ -dependent stratospheric *source* intensity). According to Vadas et al. (2019, Section 7), low solar activity leads to a rapid increase of the kinematic viscosity with height, which is favorable for generating localized and strong body force. Secondary/tertiary GWs are created by the strong body force and can propagate to the upper thermosphere, which can be finally recorded by GRACE(-FO) instrument. This mechanism may explain the strong dependence of GW intensity at GRACE(-FO) altitudes on solar activity.

Interestingly, the two solar minima (2008–2009 vs. 2019–2020) in Figure 5 exhibit different levels of upper-thermospheric GW activity (approximately by a factor of two). According to Figure 5e, the $F_{10.7}$ indices during the two solar-minimum periods are comparable to each other, but GW activity in the former period (2008–2009) is stronger than in the latter (2019–2020) in Figures 5a and 5b. Based on solar radiation data from the Solar Radiation and Climate Experiment mission, Woods et al. (2022) reported that the solar minimum in 2008–2009 and that in 2019–2020 had minimal difference from each other. Therefore, the GW activity difference between the two solar minima (Figure 5) cannot be attributed to different solar radiation or concomitantly different thermospheric heating. A plausible explanation of the GW activity difference may be the actual observation altitudes of GRACE and GRACE-FO, which were different during the two solar minimum periods. In 2008–2009, GRACE observed thermospheric mass density at ~ 470 km while in 2019–2020 GRACE-FO collected data near 500 km (Figure 1a). As lower altitudes would be more favorable for encountering GWs coming from below, the altitude difference between GRACE (2008–2009) and GRACE-FO (2019–2020) may explain the GW activity difference of a factor of two, at least in part. According to Vadas (2007, Figure 11), GW momentum flux can halve when the observation height increases by only $0.5 \sim 1$ scale height. The scale height under low solar activity was approximately 30 km in that study, which is comparable to the altitude difference between GRACE in 2008–2009 (~ 470 km) and GRACE-FO in 2019–2020 (~ 500 km). Further works including first-principle simulations are warranted to verify this estimation quantitatively.

The local time dependence of GW activity (Figures 7 and 8) can be interpreted in a similar context to that of the solar activity effect. The upper-thermospheric density is higher in the afternoon (e.g., 12–17 MLT) than in the morning (e.g., 07–12 MLT): see, for example, Liu et al. (2005, Figure 2). That is, the thermosphere is cooler in the morning than in the afternoon, like it is cooler during solar minima than in solar maxima (see also Ruan et al., 2018, Figure 1). Therefore, a similar mechanism to Vadas et al. (2019) may explain our Figures 7 and 8: that is, a colder thermosphere can promote the generation of secondary/tertiary GWs and their propagation to the upper thermosphere.

The GW activity minima being latitudinally biased toward the summer hemisphere (e.g., Figures 8d and 8f) can also be attributed to ambient upper-thermospheric density/temperature being higher in the summer hemisphere than in the winter (e.g., Thayer et al., 2012, Figures 7 and A2; Malhotra et al., 2020, Figure 5). As for the GW activity minima around 15 MLT in Figures 8d and 8f, Vadas and Azeem (2021, Section 4.4) showed that it takes about 1 hr from the thermospheric GW source (i.e., body force at ~ 140 km) to propagate to ~ 310 km. This

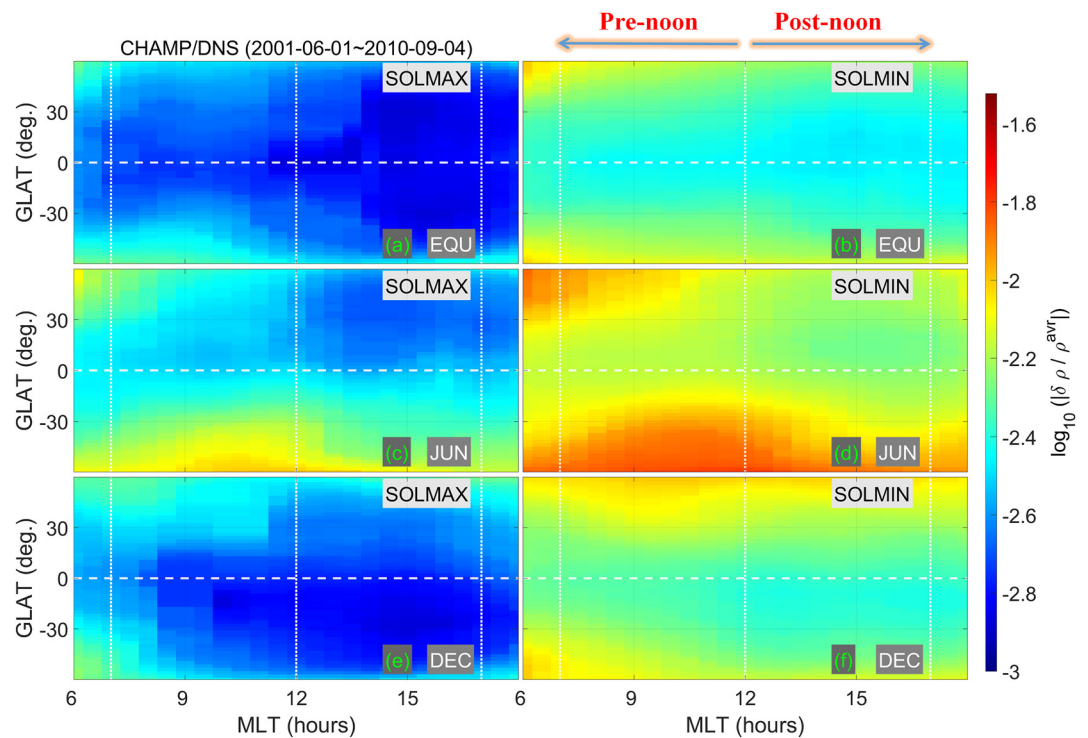


Figure 9. Similar to Figure 8, but with Challenging Minisatellite Payload data between 2001 and 2010.

time delay may, when extrapolated to the GRACE(-FO) altitudes around 500 km, explain why the GW activity minima appear at ~ 15 MLT in Figure 8, which is 1–2 hr later than the peak of background thermospheric density in previous studies: for example, 13–14 local time in Liu et al. (2005, Figure 2) and Weng et al. (2017, Figure 7).

To verify the robustness of the pre-noon/post-noon asymmetry, we demonstrate that the local time dependence of GWs as shown in Figure 8 can be replicated in the CHAMP data (~ 400 km altitude). Figure 9 is similar to Figure 8, but based on the CHAMP observations between 2001 and 2010, which were used in Park et al. (2014). The detailed GLAT dependence looks slightly different between GRACE(-FO) and CHAMP (especially during the solar minimum), which can be attributed to their unlike orbit altitudes, precession periods, and mission years. Note also that CHAMP GW activity (Figure 9) generally appears lower than that of GRACE (Figure 8) possibly due to some remaining inconsistency in the density data between different missions related to uncertainties in the modeling of the gas-surface interactions (e.g., March et al., 2021). Below, we do not quantitatively compare the CHAMP observations (Figure 9) with those of GRACE(-FO) (Figure 8), but only check their morphological consistency. In Figure 9, the pre-noon/post-noon asymmetry of CHAMP data (i.e., stronger GWs before noon than thereafter) is as conspicuous as for GRACE(-FO) observations (Figure 8). The good agreement between the CHAMP and GRACE(-FO) results supports the credibility of the conclusion that the pre-noon upper thermosphere hosts stronger GWs than its post-noon counterpart. Furthermore, Leelavathi et al. (2020, Figure 6) and England et al. (2022, Figure 4) recently showed that Martian thermospheric irregularities also prefer pre-noon hours to post-noon. Hence, the pre-noon bias may be a common phenomenon in the thermospheres of the Earth and Mars.

As an additional remark, we note that mid-latitude ($|\text{IGLAT}| > 20^\circ$) GWs in the *summer* hemisphere of Figures 8 and 9, albeit being weaker than its winter-hemisphere counterpart, exhibit a slight enhancement early in the morning (06–09 MLT). For example, a small red patch appears in the top-left corner of Figure 8c, which corresponds to mid-latitude regions of early morning MLT in the local *summer*. The feature is stronger for low solar activity. This minority population can be explained by Yamashita et al. (2013, Figure 6), where mid-latitude GWs below ~ 80 km altitude have a minor peak in the *summer* hemisphere, in addition to the major peak in the winter. The minority exists even for GWs having long vertical wavelengths (Yamashita et al., 2013, Figure 6), which are known to disturb the thermosphere more efficiently than shorter-wavelength GWs (Vadas & Fritts, 2005). Under

favorable conditions of propagation, such as a cold thermosphere in the morning under low solar activity, the minority GWs (i.e., mid-latitude GWs in the *summer* hemisphere) below 80 km height may conspicuously disturb the upper-thermosphere at CHAMP and GRACE(-FO) altitudes. Theoretical confirmation of this conjecture would be an interesting topic, which is reserved for future research.

4.2. Comparison Between *Relative* and *Absolute* Fluctuation Amplitudes

Until now, we have demonstrated that GW activity, defined as $|\delta\rho/\rho_{\text{avr}}|$ (*relative* fluctuation amplitude), prefers cold background thermosphere (i.e., low solar activity and pre-noon MLT). Then, it may be natural to ask whether the conclusion remains valid even if we use $|\delta\rho|$ (*absolute* fluctuation amplitude) instead of $|\delta\rho/\rho_{\text{avr}}|$. Figures S1 and S2 in Supporting Information S1 are the same as Figure 4 (solar activity dependence) and Figure 7 (local time dependence), respectively, but with $|\delta\rho/\rho_{\text{avr}}|$ replaced by $|\delta\rho|$. The figures demonstrate that GW activity represented by $|\delta\rho|$ (*absolute* fluctuation amplitude), generally prefers a hot background thermosphere (i.e., high solar activity and post-noon MLT) although the seasonal/longitudinal distributions resemble those of $|\delta\rho/\rho_{\text{avr}}|$: for example, mid-latitude GWs generally preferring the winter hemisphere and the hotspot near the Andes appearing in June solstice. Therefore, higher $|\delta\rho/\rho_{\text{avr}}|$ in colder background thermosphere, as was shown in Section 3, does not necessarily mean that $|\delta\rho|$, which better represents the practical impact of GWs on spacecraft acceleration/deceleration, is also larger for the colder thermosphere.

Nevertheless, the use of $|\delta\rho/\rho_{\text{avr}}|$ in our study can be justified in the following respect. First, the GW momentum flux per unit mass (in unit of m^2/s^2), which is a widely used parameter for characterizing GWs (e.g., Cao & Liu, 2022; de Wit et al., 2017; Jia et al., 2018; Vadas, 2007; Vadas & Crowley, 2017) and whose divergence is important in estimating mean flow acceleration (in unit of m/s^2 ; e.g., Tian et al., 2020), is positively correlated with $|\delta\rho/\rho_{\text{avr}}|$ rather than with $|\delta\rho|$ alone (Swenson & Liu, 1998, Equations 1 and 5). Second, most previous studies on upper-thermospheric GWs observed in situ addressed $|\delta\rho/\rho_{\text{avr}}|$ rather than $|\delta\rho|$ (e.g., Bruinsma and Forbes, 2008; Park et al., 2014; Garcia et al., 2016; Forbes et al., 2016; Liu, Pedatella, & Hocke, 2017; Liu, Yue, et al., 2017; Trinh et al., 2018; Vadas et al., 2019). Therefore, using $|\delta\rho/\rho_{\text{avr}}|$ (instead of $|\delta\rho|$) as the prime parameter helps us put our results in the context of the previous studies. Third, the total thermospheric mass density in Figures 5c and 5d is not as well correlated with $F_{10.7}$ ($|R| < 0.4$) as $|\delta\rho/\rho_{\text{avr}}|$ is ($|R| > 0.7$). The relative magnitudes of the correlation coefficients indicate that the $|\delta\rho/\rho_{\text{avr}}|$ climatology in our study does not simply reflect ρ_{avr} variability: it further justifies the use of $|\delta\rho/\rho_{\text{avr}}|$ for GW statistics.

5. Summary and Conclusions

Using thermospheric mass density measured by GRACE and GRACE-FO at altitudes mostly close to 500 km (i.e., previously unexplored heights) between 2002 and 2022 (i.e., with the longest ever data sets), we have statistically investigated *relative* fluctuation amplitudes of dayside low-/mid-latitude upper-thermospheric mass density, which we deem GW signatures coming from below. The main findings can be summarized as follows.

First, GRACE(-FO) demonstrates that GWs from below can disturb the thermosphere at least up to ~ 500 km. The seasonal/longitudinal distributions of thermospheric fluctuations in GRACE(-FO) data agree well with previous reports on GWs at CHAMP (~ 400 km) and GOCE (~ 250 km) altitudes. Specifically, the following well-known properties of the GWs are reproduced by the GRACE(-FO) data:

1. In low-latitude (e.g., $|\text{GLAT}| < 10^\circ$) regions, the GWs are stronger in continental regions than above oceans.
2. At mid-latitudes (e.g., $|\text{GLAT}| > 20^\circ$), the GWs are stronger in the winter hemisphere than in the summer hemisphere, with the hot spot near the South Atlantic/American region in June solstice.
3. The GW intensity exhibits anti-correlation with solar activity on multi-year time scales.

Second, the anti-correlation between GW activity and solar activity can also be identified on the time scale of the solar rotation period (~ 27 days).

Third, the GWs are stronger before noon than afterward, for both GRACE(-FO) and CHAMP. This feature can result from the thermospheric density being lower in the pre-noon sector than in the afternoon, which can promote the generation of secondary/tertiary GWs that penetrate upward (Vadas et al., 2019).

The GRACE-FO mission is continuing its operations at the moment, and will hopefully keep producing high-quality thermospheric data sets for the coming decades. After accumulating more data, we may tackle upper-thermospheric GW climatology on a longer time scale, for example, secular trends of their activity that may be affected by greenhouse gases.

Data Availability Statement

The GRACE and GRACE-FO data used for this study are available at the ESA's Swarm repository (<https://swarm-diss.eo.esa.int/#swarm%2FMultimission>) and the Delft University of Technology's thermosphere database (<http://thermosphere.tudelft.nl>).

Acknowledgments

JP was supported by the National Research Council of Science & Technology (NST) grant by the Korea government (MSIT) (No. CPS21161-120).

References

- Behzadpour, S., Mayer-Gürr, T., & Krauss, S. (2021). GRACE follow-on accelerometer data recovery. *Journal of Geophysical Research: Solid Earth*, 126(5), e2020JB021297. <https://doi.org/10.1029/2020JB021297>
- Bruinsma, S. L., & Forbes, J. M. (2008). Medium-to large-scale density variability as observed by CHAMP. *Space Weather*, 6(8), S08002. <https://doi.org/10.1029/2008SW000411>
- Cao, B., & Liu, A. Z. (2022). Statistical characteristics of high-frequency gravity waves observed by an airglow imager at Andes Lidar Observatory. *Earth and Space Science*, 9(6), e2022EA002256. <https://doi.org/10.1029/2022EA002256>
- Christophe, B., Boulanger, D., Foulon, B., Huynh, P.-A., Lebat, V., Liorzou, F., & Perrot, E. (2015). A new generation of ultra-sensitive electrostatic accelerometers for GRACE Follow-on and towards the next generation gravity missions. *Acta Astronautica*, 117, 1–7. ISSN 0094-5765. <https://doi.org/10.1016/j.actaastro.2015.06.021>
- de Wit, R. J., Janches, D., Fritts, D. C., Stockwell, R. G., & Coy, L. (2017). Unexpected climatological behaviour of MLT gravity wave momentum flux in the lee of the Southern Andes hot spot. *Geophysical Research Letters*, 44(2), 1182–1191. <https://doi.org/10.1002/2016GL072311>
- Doornbos, E. (2012). *Thermospheric density and wind determination from satellite dynamics*. Springer Theses. Springer-Verlag.
- Doornbos, E., Van den IJssel, J., Lühr, H., Förster, M., & Koppenwallner, G. (2010). Neutral density and crosswind determination from arbitrarily oriented multi-axis accelerometers on satellites. *Journal of Spacecraft and Rockets*, 47(4), 580–589. <https://doi.org/10.2514/1.48114>
- England, S. L., Jain, S., Deighan, J., Chaffin, M., Holsclaw, G., Evans, J. S., et al. (2022). Spatio-temporal structure of far ultraviolet Martian dayglow observed by EMM-EMUS. *Geophysical Research Letters*, 49(19), e2022GL099611. <https://doi.org/10.1029/2022GL099611>
- Ern, M., Preusse, P., Gille, J. C., Hepplewhite, C. L., Mlynczak, M. G., Russell, J. M., & Riese, M. (2011). Implications for atmospheric dynamics derived from global observations of gravity wave momentum flux in stratosphere and mesosphere. *Journal of Geophysical Research*, 116(19), 1–24. <https://doi.org/10.1029/2011JD015821>
- Forbes, J. M., Bruinsma, S. L., Doornbos, E., & Zhang, X. (2016). Gravity wave-induced variability of the middle thermosphere. *Journal of Geophysical Research: Space Physics*, 121(7), 6914–6923. <https://doi.org/10.1002/2016JA022923>
- Forbes, J. M., Bruinsma, S. L., Miyoshi, Y., & Fujiwara, H. (2008). A solar terminator wave in thermosphere neutral densities measured by the CHAMP satellite. *Geophysical Research Letters*, 35(14), L14802. <https://doi.org/10.1029/2008GL034075>
- Garcia, R. F., Bruinsma, S., Massarweh, L., & Doornbos, E. (2016). Medium-scale gravity wave activity in the thermosphere inferred from GOCE data. *Journal of Geophysical Research: Space Physics*, 121(8), 8089–8102. <https://doi.org/10.1002/2016JA022797>
- Geller, M. A., Zhou, T., & Love, P. T. (2015). Tropical gravity wave momentum fluxes and latent heating distributions. *Journal of the Atmospheric Sciences*, 72(7), 2762–2768. <https://doi.org/10.1175/jas-d-15-0020.1>
- Hocke, K., Lainer, M., Moreira, L., Hagen, J., Fernandez Vidal, S., & Schranz, F. (2016). Atmospheric inertia-gravity waves retrieved from level-2 data of the satellite microwave limb sounder Aura/MLS. *Annales Geophysicae*, 34(9), 781–788. <https://doi.org/10.5194/angeo-34-781-2016>
- Hoffmann, L., Xue, X., & Alexander, M. J. (2013). A global view of stratospheric gravity wave hotspots located with Atmospheric Infrared Sounder observations. *Journal of Geophysical Research: Atmospheres*, 118, 416–434. <https://doi.org/10.1029/2012JD018658>
- Illés-Almár, E., Almár, I., & Bencze, P. (1998). Neutral density depletions attributed to plasma bubbles. *Journal of Geophysical Research*, 103(A3), 4115–4116. <https://doi.org/10.1029/97JA02963>
- Illés-Almár, E., Almár, I., Bencze, P., & Laneve, G. (2001). Wave-like variations and sudden density decreases in the lower thermosphere as measured by the San Marco V satellite. *Physics and Chemistry of the Earth, Part C: Solar, Terrestrial & Planetary Science*, 26(4), 275–280. [https://doi.org/10.1016/S1464-1917\(00\)00120-3](https://doi.org/10.1016/S1464-1917(00)00120-3)
- Jia, M., Xue, X., Gu, S., Chen, T., Ning, B., Wu, J., et al. (2018). Multiyear observations of gravity wave momentum fluxes in the midlatitude mesosphere and lower thermosphere region by meteor radar. *Journal of Geophysical Research: Space Physics*, 123(7), 5684–5703. <https://doi.org/10.1029/2018JA025285>
- Landerer, F. W., Flechtner, F. M., Save, H., Webb, F. H., Bandikova, T., Bertiger, W. I., et al. (2020). Extending the global mass change data record: GRACE follow-on instrument and science data performance. *Geophysical Research Letters*, 47(12), e2020GL088306. <https://doi.org/10.1029/2020GL088306>
- Laundal, K. M., & Richmond, A. D. (2017). Magnetic coordinate systems. *Space Science Reviews*, 206(1–4), 27–59. <https://doi.org/10.1007/s11214-016-0275-y>
- Leelavathi, V., Venkateswara Rao, N., & Rao, S. V. B. (2020). Interannual variability of atmospheric gravity waves in the Martian thermosphere: Effects of the 2018 planet-encircling dust event. *Journal of Geophysical Research: Planets*, 125(12), e2020JE006649. <https://doi.org/10.1029/2020JE006649>
- Liu, H., Lühr, H., Henize, V., & Köhler, W. (2005). Global distribution of the thermospheric total mass density derived from CHAMP. *Journal of Geophysical Research*, 110(A4), A04301. <https://doi.org/10.1029/2004JA010741>
- Liu, H., Pedatella, N., & Hocke, K. (2017). Medium-scale gravity wave activity in the bottomside F region in tropical regions. *Geophysical Research Letters*, 44(14), 7099–7105. <https://doi.org/10.1002/2017GL073855>
- Liu, X., Yue, J., Xu, J., Garcia, R. R., Russell, J. M., Mlynczak, M., et al. (2017). Variations of global gravity waves derived from 14 years of SABER temperature observations. *Journal of Geophysical Research: Atmospheres*, 122(12), 6231–6249. <https://doi.org/10.1002/2017JD026604>
- Lühr, H., Rother, M., Köhler, W., Ritter, P., & Grunwaldt, L. (2004). Thermospheric up-welling in the cusp region: Evidence from CHAMP observations. *Geophysical Research Letters*, 31(6), L06805. <https://doi.org/10.1029/2003GL019314>

- Lühr, H., & Xiong, C. (2010). IRI-2007 model overestimates electron density during the 23/24 solar minimum. *Geophysical Research Letters*, 37(23), L23101. <https://doi.org/10.1029/2010GL045430>
- Malhotra, G., Ridley, A. J., Marsh, D. R., Wu, C., Paxton, L. J., & Mlyneczek, M. G. (2020). Impacts of lower thermospheric atomic oxygen on thermospheric dynamics and composition using the global ionosphere thermosphere model. *Journal of Geophysical Research: Space Physics*, 125(9), e2020JA027877. <https://doi.org/10.1029/2020JA027877>
- March, G., Van den IJssel, J., Siemes, C., Visser, P., Doornbos, E., & Pilinski, M. (2021). Gas-surface interactions modelling influence on satellite aerodynamics and thermosphere mass density. *Journal of Space Weather and Space Climate*, 11(54), 1–23. <https://doi.org/10.1051/swsc/2021035>
- Matzka, J., Stolle, C., Yamazaki, Y., Bronkalla, O., & Morschhauser, A. (2021). The geomagnetic Kp index and derived indices of geomagnetic activity. *Space Weather*, 19(5), e2020SW002641. <https://doi.org/10.1029/2020SW002641>
- Moffat-Griffin, T., Colwell, S. R., Wright, C. J., Hindley, N. P., & Mitchell, N. J. (2020). Radiosonde observations of a wintertime meridional convergence of gravity waves around 60°S in the lower stratosphere. *Geophysical Research Letters*, 47(20), e2020GL089740. <https://doi.org/10.1029/2020GL089740>
- Park, J., Lühr, H., Lee, C., H Kim, Y., Jee, G., & Kim, J.-H. (2014). A climatology of medium-scale gravity wave activity in the midlatitude/low-latitude daytime upper thermosphere as observed by CHAMP. *Journal of Geophysical Research: Space Physics*, 119(3), 2187–2196. <https://doi.org/10.1002/2013JA019705>
- Park, J., Lühr, H., & Min, K. W. (2010). Neutral density depletions associated with equatorial plasma bubbles as observed by the CHAMP satellite. *Journal of Atmospheric and Solar-Terrestrial Physics*, 72(2–3), 157–163. <https://doi.org/10.1016/j.jastp.2009.11.003>
- Qian, L., Burns, A. G., Solomon, S. S., Smith, A. K., McNerney, J. M., Hunt, L. A., et al. (2018). Temporal variability of atomic hydrogen from the mesopause to the upper thermosphere. *Journal of Geophysical Research: Space Physics*, 123(1), 1006–1017. <https://doi.org/10.1002/2017JA024998>
- Ruan, H., Lei, J., Dou, X., Liu, S., & Aa, E. (2018). An exospheric temperature model based on CHAMP observations and TIEGCM simulations. *Space Weather*, 16(2), 147–156. <https://doi.org/10.1002/2017SW001759>
- Siemes, C., & the TOLEOS team. (2022). TOLEOS product definition document. Retrieved from https://earth.esa.int/eogateway/documents/20142/37627/TOLEOS_Product_Definition_Document.pdf
- Song, B.-G., Song, I.-S., Chun, H.-Y., Lee, C., Kam, H., Kim, Y. H., et al. (2021). Activities of small-scale gravity waves in the upper mesosphere observed from meteor radar at King Sejong Station, Antarctica (62.22°S, 58.78°W) and their potential sources. *Journal of Geophysical Research: Atmospheres*, 126(10), e2021JD034528. <https://doi.org/10.1029/2021JD034528>
- Stolle, C., Michaelis, I., Xiong, C., Rother, M., Usbeck, T., Yamazaki, Y., et al. (2021). Observing Earth's magnetic environment with the GRACE-FO mission. *Earth Planets and Space*, 73(1), 51. <https://doi.org/10.1186/s40623-021-01364-w>
- Stolle, C., Olsen, N., Anderson, B., Doornbos, E., & Kuvshinov, A. (2021). Special issue “Characterization of the geomagnetic field and its dynamic environment using data from space-based magnetometers”. *Earth Planets and Space*, 73(1), 83. <https://doi.org/10.1186/s40623-021-01409-0>
- Swenson, G. R., & Liu, A. Z. (1998). A model for calculating acoustic gravity wave energy and momentum flux in the mesosphere from OH airglow. *Geophysical Research Letters*, 25(4), 477–480. <https://doi.org/10.1029/98gl00132>
- Thayer, J. P., Liu, X., Lei, J., Pilinski, M., & Burns, A. G. (2012). The impact of helium on thermosphere mass density response to geomagnetic activity during the recent solar minimum. *Journal of Geophysical Research*, 117(A7), A07315. <https://doi.org/10.1029/2012JA017832>
- Tian, C., Hu, X., Liu, Y., Cheng, X., Yan, Z., & Cai, B. (2020). Seasonal variations of high-frequency gravity wave momentum fluxes and their forcing toward zonal winds in the mesosphere and lower thermosphere over Langfang, China (39.4°N, 116.7°E). *Atmosphere*, 11(11), 1253. <https://doi.org/10.3390/atmos11111253>
- Trinh, Q. T., Ern, M., Doornbos, E., Preusse, P., & Riese, M. (2018). Satellite observations of middle atmosphere–thermosphere vertical coupling by gravity waves. *Annales Geophysicae*, 36(2), 425–444. <https://doi.org/10.5194/angeo-36-425-2018>
- Vadas, S. L. (2007). Horizontal and vertical propagation and dissipation of gravity waves in the thermosphere from lower atmospheric and thermospheric sources. *Journal of Geophysical Research*, 112(A6), A06305. <https://doi.org/10.1029/2006JA011845>
- Vadas, S. L., & Azeem, I. (2021). Concentric secondary gravity waves in the thermosphere and ionosphere over the continental United States on March 25–26, 2015 from deep convection. *Journal of Geophysical Research: Space Physics*, 126(2), e2020JA028275. <https://doi.org/10.1029/2020JA028275>
- Vadas, S. L., & Crowley, G. (2017). Neutral wind and density perturbations in the thermosphere created by gravity waves observed by the TIDDBIT sounder. *Journal of Geophysical Research: Space Physics*, 122(6), 6652–6678. <https://doi.org/10.1002/2016JA023828>
- Vadas, S. L., & Fritts, D. C. (2005). Thermospheric responses to gravity waves: Influences of increasing viscosity and thermal diffusivity. *Journal of Geophysical Research*, 110(D15), D15103. <https://doi.org/10.1029/2004JD005574>
- Vadas, S. L., Xu, S., Yue, J., Bossert, K., Becker, E., & Baumgarten, G. (2019). Characteristics of the quiet-time hot spot gravity waves observed by GOCE over the Southern Andes on 5 July 2010. *Journal of Geophysical Research: Space Physics*, 124(8), 7034–7061. <https://doi.org/10.1029/2019JA026693>
- Van den IJssel, J. A. A. (2014). *GPS-based precise orbit determination and accelerometry for low flying satellites* (Ph. D. Thesis). Technische Universiteit Delft.
- Weng, L., Lei, J., Sutton, E., Dou, X., & Fang, H. (2017). An exospheric temperature model from CHAMP thermospheric density. *Space Weather*, 15(2), 343–351. <https://doi.org/10.1002/2016SW001577>
- Woods, T. N., Harder, J. W., Kopp, G., & Snow, M. (2022). Solar-cycle variability results from the solar radiation and climate experiment (SORCE) mission. *Solar Physics*, 297(4), 43. <https://doi.org/10.1007/s11207-022-01980-z>
- Xu, S., Vadas, S. L., & Yue, J. (2021). Thermospheric traveling atmospheric disturbances in austral winter from GOCE and CHAMP. *Journal of Geophysical Research: Space Physics*, 126(9), e2021JA029335. <https://doi.org/10.1029/2021JA029335>
- Yamashita, C., England, S. L., Immel, T. J., & Chang, L. C. (2013). Gravity wave variations during elevated stratopause events using SABER observations. *Journal of Geophysical Research: Atmospheres*, 118(11), 5287–5303. <https://doi.org/10.1002/jgrd.50474>